ACS OMEGA

Article

Cite This: ACS Omega 2019, 4, 4658−4670

http://pubs.acs.org/journal/acsodf

Anodic Oxidation of Butan-1-ol on Reduced Graphene Oxide-Supported Pd−Ag Nanoalloy for Fuel Cell Application

Ankita Mahajan,[†] Senjuti Banik,[†] Dipanwita Majumdar,[‡] and Swapan Kumar Bhattacharya*[,†]

[†]Physical Chemistry Section, Department of Chemistry, Jadavpur University, Kolkata, 700 032 West Bengal, India

[‡]Department of Chemistry, Chandernagore College, Chandannagar, Hooghly, 712136 West Bengal, India

Supporting Information

ABSTRACT: Reduced graphene oxide (RGO)-supported bimetallic Pd_xAg_y alloy nanoparticles of various compositions were synthesized by one-pot coreduction of respective precursors with hydrazine for use in the anode catalysis of oxidation of butan-1-ol in alkali. The as-synthesized catalyst materials were characterized by microscopic, spectroscopic, and diffraction techniques. Cyclic voltammetry (CV), chronoamperometry, and polarization studies infer that a few Pd_xAg_y materials exhibit an enhanced and synergistic catalytic activity in reference to Pd and Ag nanomaterials. Among the various RGO composites of Pd_xAg_y alloy on graphite support, the one containing the $Pd_{70}Ag_{30}$@RGO composite is the best in catalytic activity. The cycle life of the catalyst is found to be very high, and PdO and Ag_2O are found to be generated in the catalyst material with little change in the catalytic capability during the 100th cycle of CV operation. The addition of Ag upto 30 atom % in the Pd_xAg_y alloy causes greater formation of butyraldehyde and butyl butanoate among the various products. Larger atom % of Pd helps to form sodium butyrate and sodium carbonate, as evident from the ex situ Fourier transform infrared and high-performance liquid chromatography study of the product mixtures and the separate CV studies of the intermediate products. A suitable mechanism is also proposed to fit the findings.

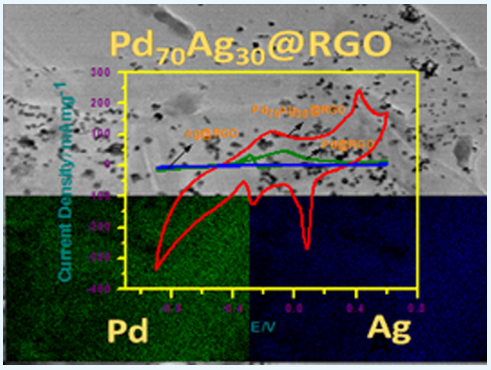

INTRODUCTION

In the era of rapidly depleting fossil fuel and ever-rising demand for renewable and sustainable energy, the urge for environment-safe fuel source and its proper utilization has become an immediate concern for the modern society.[1] Direct alcohol fuel cells (DAFCs) appear as potential alternative green and renewable power devices, as these use liquid fuels, which are harmless, easy to handle, and easy to store as well as affable to the ecosystem.[2,3] In addition, these devices possess higher volumetric energy densities than the gaseous hydrogen counterparts, thereby becoming more popular as highly efficient, low-emissive, and soundless power sources for cars and portable electronic devices.[4]

Various alcohols such as methanol, ethanol, propanol-isomers, ethane-1,2-diol, and propane-1,2,3-triol have been widely investigated as potential fuels for DAFCs.[5−10] The reactivity of small primary alcohols on the Pt electrode surface in acid has been found to follow the order methanol > ethanol > propanol > *n*-butanol.[5,11] However, the poor alcohol cross-over across the membrane and the complex reaction mechanism lower the cell performance, and these are the major hurdles in the alcohol oxidation process in most cases.[12] Nonetheless, recent studies reveal that the alcohol cross-over rate is comprehensively reduced on increasing the alcohol chain length.[12] Moreover, a single alcohol molecule bears one oxygen atom only; thus, the full oxidation of alcohol to carbon dioxide requires additional O atom, which is provided by water or water-adsorbed residue (OH_{ads}) on the metal-catalyst surface. Again, the oxidation of water on the metal surface is an energy-seeking process that upraises the anodic over potential of DAFCs. Thus, the present objective lies in full oxidation of the alcohol molecule at a lower anodic potential to attain high fuel cell efficiency.[5,13−15]

Various other important factors such as easy availability, accessibility, price, environmentally benign, and sustainability are important criteria for selecting a suitable fuel for DAFCs.[16] A thorough knowledge about the kind of intermediates, the effective cell voltage, and the amount of deliverable charge per fuel molecule is necessary for the fruitful fabrication of a fuel cell.[17] Methanol is comparatively easier to oxidize, but toxicity, inflammability, and nonavailability of the renewable source restrict its usage in practical DAFCs.[18] In contrast, ethanol is nontoxic and easily processable from sugar fermentations.[19−22] However, the utilization of edible food-based biomass feed stock for generation of large-scale bioethanol has been a sensitive issue of significant debate in the recent days.[23,24] In this regard, butanol may be considered as a suitable alternative with higher energy density and better infrastructure compatibility. Currently, it is employed as a gasoline additive as well.[24−26] Furthermore, it is less poisonous, noncorrosive, and

Received: December 19, 2018
Accepted: February 8, 2019
Published: March 4, 2019

DOI: 10.1021/acsomega.8b03561
ACS Omega 2019, 4, 4658−4670

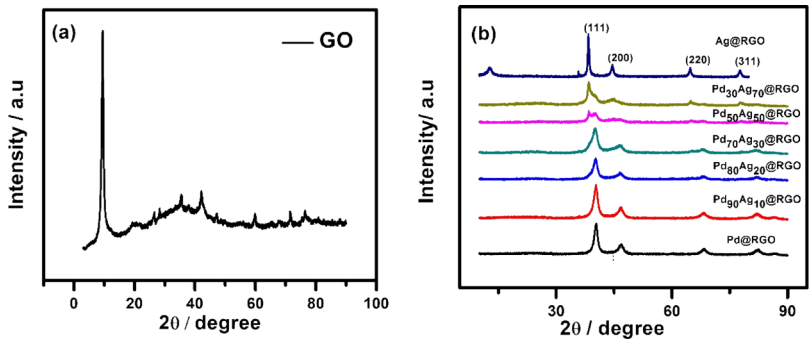

Figure 1. PXRD patterns for (a) GO and (b) all synthesized nanocomposite materials.

biodegradable and causes less soil and water pollution.[27] Works based on butanol oxidation reaction (BOR), unlike that of methanol and ethanol, have been much less explored. The oxidation of butanol isomers on various electrodes (Pt, Au, Pd, and Rh polycrystalline electrodes) in alkaline media was studied in the recent past.[9,28,29]

Research reveals that the Pd catalyst has been considered as an excellent material for the construction of the anode for application of DAFCs in alkaline media.[30,31] First, palladium exhibits better electrocatalytic activity and poison tolerance than platinum for alkaline oxidation of alcohols. Second, Pd is relatively more copious compared to Pt, which makes it more cost effective. However, Pd-based electrocatalysts need additional enhancement in catalytic performance and stability to accomplish commercialization of DAFCs.[32]

Bimetallic catalysts generally exhibit superior activity over monometallic catalysts for alcohol oxidation reactions because of the bifunctional mechanism and/or ligand effect.[33] Significant efforts have been made to improve the performance of Pd catalysts by combining with one or more elements, such as Au, Ag, Ni, Cu, Sn, Pb, and so forth, to improve the capability of Pd for alkaline alcohol electro-oxidation.[26,33−36] Open-structural effects along with excellent surface accessibility with the optimal use of precious metals are also obtained by this technology.

A variety of approaches associated with the preparation of bimetallic catalysts, including thermal decomposition, galvanic replacements, solvothermal technique, radiolysis, electrochemical deposition, and so forth, are available in the literature.[37−39] Current research stresses on the green synthesis of alloy nanoparticles and avoids toxicity of the precursor chemicals. Our group also obtained interesting results on alcohol oxidation in alkaline medium involving green method of preparation of Pd−Ag bimetal catalysts.[40]

In the recent past, various forms of nanoporous carbons such as active carbon, carbon nanocoils, carbon nano-onions, carbon nanofibers, carbon nanotubes (CNTs), and especially graphene have been widely employed to reduce the agglomeration effect of nanoparticles besides improving their electrical conductivity, which ultimately pertains to enhancement of the overall performance of the system.[41−43] Chemical doping is essentially carried out to modify the surface structure and physicochemical property of graphene.[43,44] Incorporation of electron-rich oxygen atoms into graphene as in reduced graphene oxide (RGO) improves the dispersion state of the metal nanoparticles on the graphene surface and also modifies the surface structure of the carbon material.[44,45] RGO composites with metal nanoparticles have received significant attention in recent years because of their unique electronic, physical, mechanical, thermal, and chemical properties.[45,46]

Lately, bimetallic carbon (Pd−Ag/C) systems have exhibited excellent fuel cell efficiency with enhanced CO tolerance and better stability compared to Pt−C and Pd−C composites.[47] Even activated CNT-supported Pd−Ag (1:1) catalyst showed larger electroactive surface area and better catalytic efficiency for methanol oxidation in alkaline media.[48] Bimetallic Pd−Ag catalysts prepared by the impregnation−reduction method exhibited improved catalytic activities for ethanol oxidation reaction, a very important reaction for fuel cells.[49] Even one-pot synthesis of electrocatalysts, Pd−Ag nanoparticles decorated on RGO (synthesized using ionic liquid-assisted electrochemical exfoliation of graphite), was reported for the alkaline ethanol oxidation process.[50] Graphene-bimetallic composite systems are, thus, promising candidates for application in DAFCs.

However, to the best of our knowledge, there is no report on the comparison of the activity of BOR on bimetallic catalysts of various compositions anchored onto RGO support. In the present work, we have synthesized separate samples of Pd, Ag, and Pd_xAg_y alloy nanoparticles on the RGO matrix by coreduction of the respective metal precursor and GO with hydrazine at 60 °C. The drop-casted as-synthesized materials on graphite electrodes are used as anode catalysts for butanol oxidation in alkali. The synergetic effect of RGO and bimetallic nanosystem on the electro-oxidation of butan-1-ol has been studied in detail and is presented here. The plausible mechanism of butanol oxidation on these electrocatalysts has also been explored. Ex situ Fourier transform infrared (FTIR) and high-performance liquid chromatography (HPLC) studies of the products of BOR were carried out to understand the role of individual components in the various stages of electrocatalysis. The exploration focuses on shaping the optimum binary composition of the Pd−Ag alloy system anchored onto the RGO surface to get the best electrocatalytic activity in reference to the butan-1-ol oxidation in alkaline media.

RESULTS AND DISCUSSION

X-ray Diffraction Study. Figure 1 shows the powder X-ray diffraction (PXRD) patterns of GO and synthesized composites: Pd@RGO, $Pd_{90}Ag_{10}$@RGO, $Pd_{80}Ag_{20}$@RGO, $Pd_{70}Ag_{30}$@RGO, $Pd_{50}Ag_{50}$@RGO, $Pd_{30}Ag_{70}$@RGO, and Ag@RGO. In Figure 1a, the formation of GO has been indicated by the diffraction peak on the 2θ scale at ∼10.38° representing its (002) planes. The peak around 42.5° corresponds to the hexagonal structure of carbon, well in agreement with the literature.[41]

DOI: 10.1021/acsomega.8b03561
ACS Omega 2019, 4, 4658−4670

Table 1. PXRD Parameters and Compositions of the Synthesized Nanocrystals

electrodes	position of 2θ (degree)	d-spacing (Å) (from XRD)	crystallite size (nm)	cell parameter (Å)	evaluated atomic % of Ag in Pd_xAg_{100-x} from XRD	evaluated atomic % of Ag in Pd_xAg_{100-x} from EDX
Pd@RGO	40.63	2.219	9	3.87	0	
	46.95					
$Pd_{90}Ag_{10}$@RGO	40.35	2.235	8	3.86	11	11.9
	46.79					
$Pd_{80}Ag_{20}$@RGO	40.07	2.248	8	3.88	23	21.6
	46.58					
$Pd_{70}Ag_{30}$@RGO	40.07	2.25	6	3.89	28	31.3
	46.58					
$Pd_{50}Ag_{50}$@RGO	38.67	2.28	32	4.04	51	51.3
	45.15					
$Pd_{30}Ag_{70}$@RGO	38.40	2.31	15	4.07	75	
	44.95					
Ag@RGO	38.40	2.343	23	4.07	100	
	44.59					

The crystalline structure of the Ag@RGO, Pd@RGO, and Pd_xAg_y@RGO nanocomposites prepared by using equivalent experimental condition has been depicted by PXRD studies presented in Figure 1b. Pristine Pd and Ag samples show peaks at 40.1 (111), 46.7 (200), 68.1 (220), 82.1 (311), and 86.6 (222) and at 38.2 (111), 44.4 (200), 64.6 (220), 77.6 (311), and 81.7 (222) as found from the JCPDS files numbered 894897 and 870720, respectively. Every profile consists of at least four prominent diffraction peaks, which can be indexed as (111), (200), (220), and (311) planes of face-centered cubic structure of metallic Ag@RGO, Pd@RGO, and Pd_xAg_y@RGO nanocomposites.

The presence of relatively intense peak for Pd(111) in the composites clearly indicates that this surface would play a crucial role in the alkali-mediated alcohol oxidation process, as observed from the density functional theory calculation reported in the literature.[51] Additionally, the diffraction peaks of the bimetallic particles show characteristic shift in positions with respect to pure Ag@RGO and Pd@RGO. This observation signifies that Pd_xAg_y@RGO nanocomposites are constituted of bimetallic single phase of Pd_xAg_y alloy nanoparticles rather than two monometallic single phases of Pd and Ag nanoparticles. Moreover, the peak at ∼10° observed for GO is permanently absent; the development of a broad hump around 25° indicates instead its reduction to RGO phase (Figure S-1). Thus, the above analyses suggest that the Pd_xAg_y@RGO composite is composed of Pd_xAg_y nanoalloy anchored onto the RGO surface.

Detailed PXRD pattern analyses were carried out to obtain the values of crystallite size, lattice parameters, and mutual binary composition of Pd and Ag in Pd_xAg_y@RGO alloy nanoparticles following our previous studies[52,53] and are presented in Table 1. The atom % of Ag in the binary Pd_xAg_{100-x} alloy evaluated from the X-ray diffraction (XRD) study is found to be very close to that obtained from the energy-dispersive X-ray spectroscopy (EDX) study. The slight difference between the two data might be due to incomplete alloy formation or statistical difficulties in the measurements. The mean size of the nanoparticles was designed from the peak width at half-maximum corresponding to (111) plane by the Debye Scherrer equation. It is observed that the $Pd_{70}Ag_{30}$@RGO composite has the smallest crystallite size among all samples. According to the d-band center theory, the smaller lattice constant of Pd (3.89 Å), compared to Ag (4.09 Å), causes a tensile strain in the structure of the palladium surface on alloying Pd with Ag. This modifies the d-band center of Pd, leading to stronger adsorption ability of the hydroxyl groups, and facilitates the electro-oxidation reaction of alcohol on the metal surface.[54−56] Thus, the synergistic interaction between Ag and Pd on the RGO support in the composite is expected to exhibit enhanced electrocatalytic activity.

Morphology Study. Figure 2 represents the field emission scanning electron microscopy (FESEM) images of graphene-supported, synthesized bimetallic nanoparticles, namely (a) $Pd_{70}Ag_{30}$@RGO, (b) $Pd_{50}Ag_{50}$@RGO, (c) $Pd_{30}Ag_{70}$@RGO, and (d) Pd@RGO, respectively. On increasing the content of Ag, agglomeration of nanoparticles as well as RGO sheets is observed in the composites.

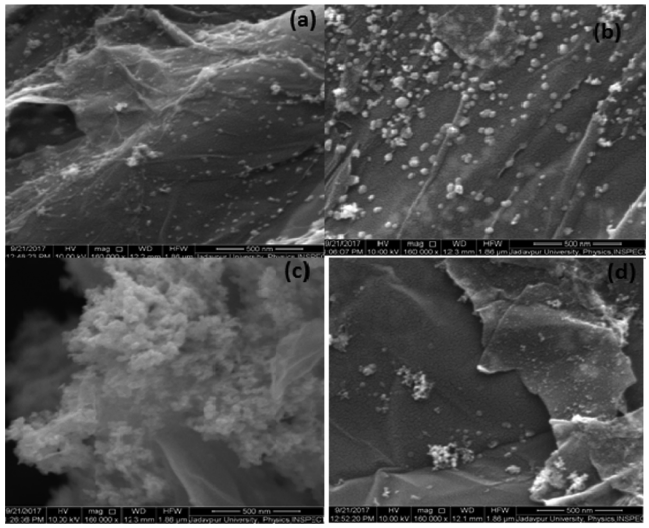

Figure 2. FESEM images of (a) $Pd_{70}Ag_{30}$@RGO, (b) $Pd_{50}Ag_{50}$@RGO, (c) $Pd_{30}Ag_{70}$@RGO, and (d) Pd@RGO samples.

The images reveal that $Pd_{70}Ag_{30}$@RGO (Figure 2a) contains thin layers of RGO with a uniform distribution of nanoparticles throughout the sheet as compared to $Pd_{30}Ag_{70}$@RGO (Figure 2c) and $Pd_{50}Ag_{50}$@RGO (Figure 2b).

Figure 3 explains the EDX spectrum with elemental composition of a part of the $Pd_{70}Ag_{30}$@RGO electrode surface. The elemental distribution of Ag and Pd in the $Pd_{70}Ag_{30}$@

DOI: 10.1021/acsomega.8b03561
ACS Omega 2019, 4, 4658−4670

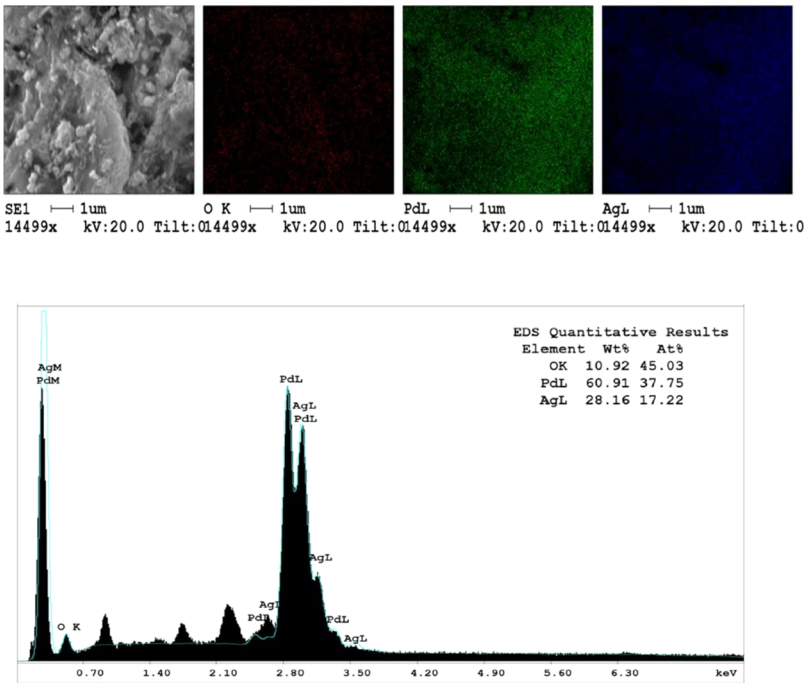

Figure 3. EDX mapping images of the $Pd_{70}Ag_{30}$@RGO composite.

RGO nanocomposite was calculated through compositional line profiles and EDX mapping analysis.

The elemental mapping indicates that both Ag and Pd are homogeneously scattered throughout the $Pd_{70}Ag_{30}$@RGO nanocomposite, further approving the possibility of alloy formation in the system.

Formation of alloy is important because it can provide the basis for higher performance of the electrocatalytic process.[57]

Transmission electron microscopy (TEM) micrograph presented in Figure 4a shows that the nanoalloy particles in

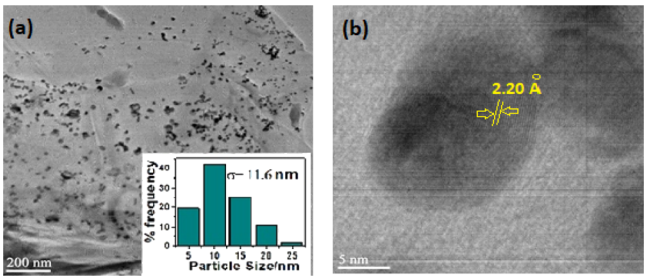

Figure 4. TEM (a) and HRTEM (b) images of the $Pd_{70}Ag_{30}$@RGO sample. Inset of (a) represents the histograms of particle size distribution.

the $Pd_{70}Ag_{30}$@RGO sample are uniformly distributed over the crumpled sheets of few-layered RGO. The average diameter of the particles as obtained from the histogram presented in the inset of the figure is found to be 11.6 nm, which is approximately double the average size of the crystallites, as obtained from XRD studies, because of agglomeration. The high-resolution TEM (HRTEM) image of the nanocomposite shows a lattice fringe spacing of 2.2 Å (Figure 4b), which closely matches with the *d*-spacing of the Pd−Ag nanoalloy composite observed from the XRD data.

Raman Spectroscopy. Raman spectroscopy is extensively utilized to analyze the carbon composite materials and can afford useful information regarding the extent of disorder, defect density, structural defect, and degree of doping levels. Figure 5 shows the Raman spectra of GO, $Pd_{70}Ag_{30}$@RGO,

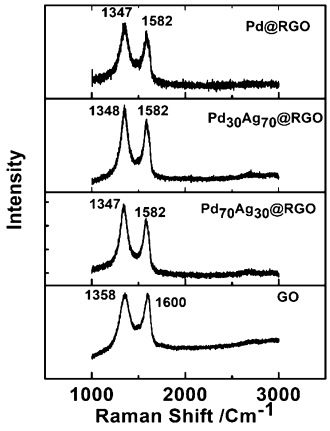

Figure 5. Raman spectra of GO, $Pd_{70}Ag_{30}$@RGO, $Pd_{30}Ag_{70}$@RGO, and Pd@RGO.

$Pd_{30}Ag_{70}$@RGO, and Pd@RGO. Generally, Raman spectrum of graphene is considered to have two main features, the G band (usually observed at ~1575 cm^{-1}) arising from the planar vibration of sp^2-bonded carbon atoms and the D band (positioned around 1350 cm^{-1}) from the vibrations of sp^3-bonded carbon atoms. The latter is related to special shaped edges, stacking disorder between two layers, and atomic defects within the layer of disordered graphene. The relative intensity ratio of D band (I_D) to G band (I_G) provides the in-plane crystallite size or the amount of disorder in the sample. All four samples exhibited the characteristic D and G bands with a slight shift in the peak positions, which are attributed to the change in electronic states in graphene owing to strong anchoring of Pd−Ag nanoparticles. The I_D/I_G ratio is found to be the highest in $Pd_{70}Ag_{30}$@RGO (1.13) followed by

DOI: 10.1021/acsomega.8b03561
ACS Omega 2019, 4, 4658−4670

$Pd_{30}Ag_{70}$@RGO (1.11), Pd@RGO (1.06), and GO (0.996) in the order, revealing a substantial reduction of sp^3-bonded carbon atoms in the composites compared to GO. Thus, the composite with more defect-free phases would accelerate faster electron transfer for electrocatalytic reactions.

Moreover, increase in the relative intensity ratio also signifies substantial chemical interaction between anchored metal nanoparticles and surface vacancies and defects on graphene sheets resulted from the chemical reduction of GO.[58,59] These features are vital for reducing the rate of agglomeration of metal nanoparticles and improving the electrocatalytic properties of the composite.

FTIR Analysis. FTIR (Figure 6) was carried out to study the chemical association of Pd−Ag with the RGO surface, supplementing the above-discussed Raman analysis.

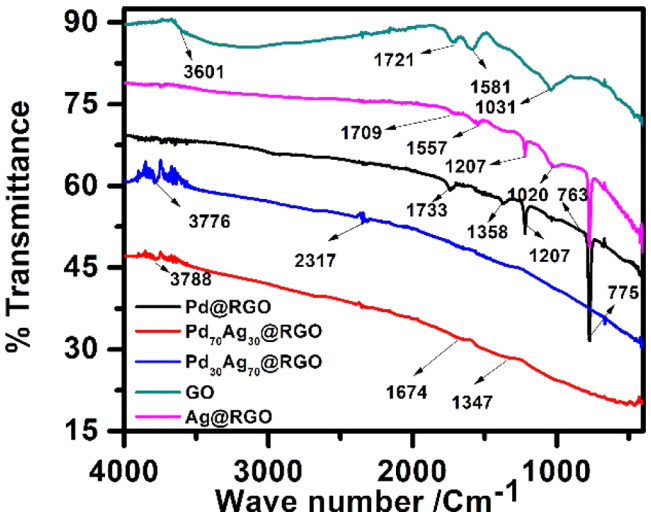

Figure 6. FTIR spectra of GO, Pd@RGO, Ag@RGO, and Pd_xAg_y@RGO samples.

FTIR spectrum of the GO sample shows typical broad, extended, and intense stretching of the hydroxyl group at 3301 cm^{-1}, and the associated red shift in the position of absorption peak is due to the involvement of O−H bonds in hydrogen bonding. In addition, peaks related to C═O carbonyl stretching observed at 1726 cm^{-1}, the aromatic C═C in conjugation with C═O group stretching at 1581 cm^{-1}, the C−O epoxy stretching at 1400 cm^{-1} and C−O alkoxy stretching frequencies at 1210 and 1031 cm^{-1}, are well in accordance with previous reports.[60]

In the spectrum of Pd@RGO and Ag@RGO, there is a decrease in relative peak intensities as well as a bathochromic shift in the positions of carboxyl, epoxy, and hydroxyl peaks. In Pd_xAg_y@RGO, further loading of metal nanoparticles dramatically modified the aforesaid peaks with the increasing removal of oxygen-containing functionalities from the surface of RGO. The study indicates the anchoring of the metal nanoalloy particles to RGO sheets vide these oxygen functionalities, thereby confirming the formation of the true composite in the above systems.

Thermogravimetric Analysis. Figure 7 illustrates the thermogravimetric analysis (TGA) profile of GO (black line), Pd@RGO (red line), and $Pd_{70}Ag_{30}$@RGO (blue line) samples, respectively. TGA profile of GO (black line) shows initial weight loss around 120 °C because of the presence of physically adsorbed water in the sample. Second degradation of

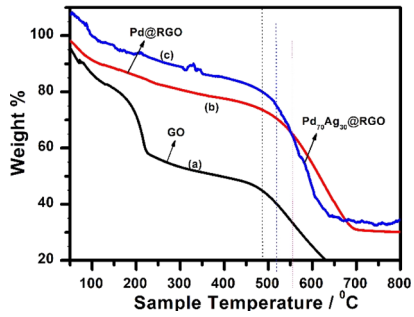

Figure 7. Thermogravimetric profiles of synthesized (a) GO, (b) Pd@RGO, and (c) $Pd_{70}Ag_{30}$@RGO composites.

GO occurs (upto 5%) at around 200 °C because of loss of oxygen-containing groups, while the third step degradation ∼500 °C is due to gradual loss of the carbon skeleton. For the Pd@RGO sample (red line), on account of Pd anchoring onto the RGO surface, initial weight loss due to physically adsorbed water and loss of oxygen-containing groups are considerably checked. This indicates that Pd preferentially is anchored to the oxygen functional groups onto the RGO surface. In the $Pd_{70}Ag_{30}$@RGO nanocomposite sample, because of further increase in the metal content compared to Pd@RGO, initial loss due to physically adsorbed water as well as loss of oxygen containing groups are further restricted. However, high exfoliation of the RGO sheets in this case renders lower decomposition temperature compared to Pd@RGO. So, the above studies confer the formation of a true composite with reasonably higher thermal stability that may be useful for higher temperature electrocatalytic applications.

Electrochemical Studies. Figure 8a represents the cyclic voltammograms of Pd@RGO, Ag@RGO, and the different Pd_xAg_y@RGO electrodes immersed in N_2-saturated 0.1 M NaOH solution. The cyclic voltammetry (CV) profile for RGO (as presented in the upper inset of Figure 8a) indicates change in the capacitance current density with potential because of adsorption and desorption of ions on the RGO sheets. It shows no characteristic peak for any redox reaction, indicating that RGO does not contain any potential redox group in the potential range studied. The CV profile for Ag@RGO electrode shows almost similar behavior to our earlier study of Ag electrodes with peak potentials at ca. 0.296 and 0.380 V for the formation of AgOH and Ag_2O, respectively.[40] Two peaks developed at around 0.03 and 0.35 V in the cyclic voltammogram for the Pd@RGO electrode are attributed to OH^- ion adsorption on the Pd surface as designated by s-PdOH and formation of oxide, s-PdO, following equations described in the previous study.[57,61] Because the peak potential of formation of PdO is slightly greater than the peak potential of AgOH formation, the two peaks sometimes often merge to a single broad peak, as observed in Pd_xAg_y@RGO electrodes. Because the peak current density for formation of s-PdOH on different electrodes follows the order $Pd_{30}Ag_{70}$@RGO > $Pd_{80}Ag_{20}$@RGO > $Pd_{70}Ag_{30}$@RGO > $Pd_{50}Ag_{50}$@RGO > Pd@RGO > $Pd_{90}Ag_{10}$@RGO, it indicates that the product s-PdOH undergoes transmetallation reaction as

$$\text{s-PdOH} + \text{Ag} = \text{AgOH} + \text{s-Pd} \quad (1)$$

Moreover, the peak current densities for the formation of PdO and Ag_2O on some Pd_xAg_y@RGO electrodes are greater than those on Ag@RGO electrode, indicating different transmetallation reactions according to the equations

DOI: 10.1021/acsomega.8b03561
ACS Omega 2019, 4, 4658−4670

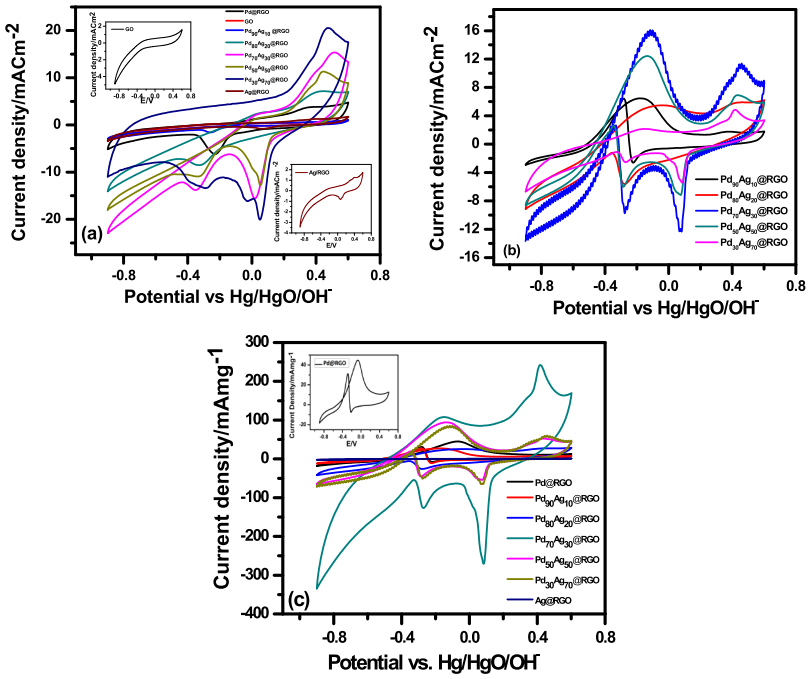

Figure 8. (a) Cyclic voltammograms of different Pd_xAg_y@RGO electrodes immersed in 0.1 M NaOH solution. The upper and lower insets of the figure represent CV curves of GO and Ag@RGO. CV curve of different electrodes of various compositions immersed in 0.1 M butanol in 0.1 M NaOH when the current scale is presented in (b) mA cm^{-2} and (c) in mA/mg. The inset of (c) depicts the CV curve of Ag@RGO taken in the same solution.

Table 2. Peak Potentials (E_F and E_B), Peak Current Density, and Other Related Parameters Obtained from CV Studies of Different Pd_xAg_y@RGO Nanoalloy Electrodes Immersed in 0.1 M Butan-1-ol in 0.1 M NaOH Solution at Room Temperature

electrodes	ECSA (cm^2 mg^{-1} of Pd)	E_F (V)	I_F (mA cm^{-2})	I_F (mA mg^{-1})	E_B (V)	I_B (mA cm^{-2})	I_g (mA mg^{-1})
Pd@RGO	28.01	−0.06	12.03	44.78	−0.285	8.25	31.04
$Pd_{90}Ag_{10}$@RGO	18.85	−0.166	6.48	26.74	−0.281	6.36	26.53
$Pd_{80}Ag_{20}$@RGO	104.4	−0.053	5.51	25.21	−0.355	−1.17	−5.72
$Pd_{70}Ag_{30}$@RGO	135.38	−0.108	15.99	105.98	−0.343	2.27	−54.22
$Pd_{50}Ag_{50}$@RGO	167.74	−0.130	12.39	93.24	−0.343	2.51	18.97
$Pd_{30}Ag_{70}$@RGO	370.86	−0.156	2.15	83.24	−0.325	−1.08	12.92
Ag@RGO	0.170	0.398	1.27	0.685	0.071	−0.8	−0.510

$$Pd + 2AgOH = PdO + H_2O + 2Ag \quad (2)$$

$$Pd + Ag_2O = PdO + Ag \quad (3)$$

as described earlier for Pd_xAg_y electrodes.[40] Thus, AgOH and Ag_2O may act as storer and supplier of oxygen to Pd.

The CV profiles (Figure 8a) for different Pd_xAg_y@RGO electrodes resemble the pure Pd_xAg_y electrodes immersed in the same solution without RGO in certain features like peaks for electro-oxidation of Pd and Ag on the electrode surface.[40]

Peak for Nafion-covered reduced graphite oxide electrode was not found, indicating that the supporting material graphite oxide and Nafion are inactive in the potential range in alkali. During the forward sweep around 0.1 V, a peak arises due to the adsorption of OH^- ion by Pd nanoparticle electrodes and formation of PdO following the equation

$$Pd + OH^- = Pd - OH_{ads} + e^- \quad (4)$$

$$Pd - OH_{ads} + OH^- = Pd - O + H_2O + e^- \quad (5)$$

After that, a shoulder and a peak are generated because of the formation of AgOH and Ag_2O, following the reactions

$$Ag + OH^- = AgOH + e^- \quad (6)$$

$$2Ag + 2OH^- = Ag_2O + H_2O + 2e^- \quad (7)$$

The peak current densities for the reactions 6 and 7 increase in the order of catalyst: $Pd_{30}Ag_{70}$@RGO > $Pd_{70}Ag_{30}$@RGO > $Pd_{50}Ag_{50}$@RGO > $Pd_{80}Ag_{20}$@RGO > $Pd_{90}Ag_{10}$@RGO for increase of Ag content in the alloys.

In the reverse scan, the first cathodic peak appears at ca. 0.05 V because of the reaction 7 occurring in the backward direction. The next reverse peak is attributed to the formation of Pd from Pd−O following the equations corresponding to eqs 4 and 5. The electrochemical surface area (ECSA) per unit mass is obtained by dividing the loading in mg cm^{-2} to the charge required per unit area to reduce monolayer of PdO divided by the value of 0.405. micro cm^{-2}.[52] The ECSA is found to follow the order $Pd_{30}Ag_{70}$@RGO > $Pd_{50}Ag_{50}$@RGO > $Pd_{70}Ag_{30}$@RGO > $Pd_{80}Ag_{20}$@RGO > Pd@RGO > $Pd_{90}Ag_{10}$@RGO, indicating that the electrodes containing a low Pd % have higher ECSA measured in cm^2 per mg of Pd. Thus, it reveals the strong interconversion between AgOH and PdOH during the reduction of PdOH/PdO.

CV Study of Butan-1-ol Oxidation in Alkali. Figure 8b compares the steady CVs of different Pd_xAg_y@RGO electrodes for the oxidation of butanol in the potential range of −0.9 to

DOI: 10.1021/acsomega.8b03561
ACS Omega 2019, 4, 4658−4670

+0.6 V at a scan rate of 0.05 V s^{-1}. A large peak for butan-1-ol oxidation appears in the potential range of −0.053 to −0.166 V during the anodic scan. The oxidation peak in the reverse (I_B) scan is due to the removal of carbonaceous species that are not entirely oxidized on the forward scan and also due to oxidation of butanol by fresh adsorption. The peak potentials and peak current densities are listed in Table 2.

The mass normalized peak current densities (I_F and I_B) illustrate that $Pd_{70}Ag_{30}$@RGO is the best catalyst among the electrodes studied. The enhanced electrocatalytic activity of $Pd_{70}Ag_{30}$@RGO toward butan-1-ol oxidation in alkali can be attributed to the presence of Ag in the alloy that can accelerate the oxidation of reaction intermediates by the formation of Ag_2O and AgOH, which can serve as a storing material of $Pd(OH)_x$. Thus, the combination with Ag reduces the poisoning of active Pd sites more effectively.

The E_F values follow the order $Pd_{80}Ag_{20}$@RGO > $Pd_{70}Ag_{30}$@RGO > $Pd_{50}Ag_{50}$@RGO > $Pd_{30}Ag_{70}$@RGO > $Pd_{90}Ag_{10}$@RGO, indicating the greater extent of oxidation of carbonaceous species relative to hydrogen in the oxidation of butan-1-ol on the electrodes.[62] Notably, E_B values follow exactly the reverse order indicating the improvement of Pd^{2+} in the oxidation of butanol and hence its delayed reduction as follows: $Pd_{70}Ag_{30}$@RGO > $Pd_{50}Ag_{50}$@RGO > $Pd_{90}Ag_{10}$@RGO > $Pd_{80}Ag_{20}$@RGO > $Pd_{30}Ag_{70}$@RGO in mA cm^{-2} and the order $Pd_{70}Ag_{30}$@RGO > $Pd_{50}Ag_{50}$@RGO > $Pd_{30}Ag_{70}$@RGO > $Pd_{90}Ag_{10}$@RGO > $Pd_{80}Ag_{20}$@RGO in mA mg^{-1} of Pd.

Chronoamperometric Study. To assess the constancy in catalytic activity and long-term stability of different Pd_xAg_y@RGO electrodes in a working butan-1-ol fuel cell, chronoamperometric (CA) measurements were carried out at a potential of −0.3 V for 600 s in a solution of 0.1 (M) 1-butanol in 0.1 (M) NaOH, as presented in Figure 9. All catalysts reveal

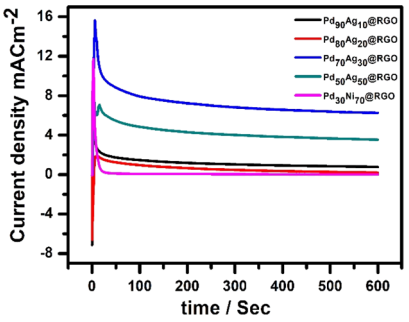

Figure 9. CA profiles of the different Pd_xAg_y@RGO electrodes immersed in 0.1 M butanol in 0.1 M NaOH.

typical profiles of decreased current density with time for alcohol oxidation. The initial high current density arises because of double-layer charging, and then the current density gets decreased for blocking of active sites on the catalyst surface because of the formation of intermediate carbonaceous species, such as CO-like species. However, all catalysts show a consistent steady current density after 600 s, indicating their possible application as a long-term constant power source. Among all catalysts, $Pd_{70}Ag_{30}$@RGO shows the maximum current density, indicating its superiority over other similarly synthesized catalysts.

Polarization Study. Figure 10 illustrates the Tafel plot of potential (E) versus logarithm of current (log i) for different alloy electrodes studied. The $Pd_{90}Ag_{10}$@RGO electrode shows

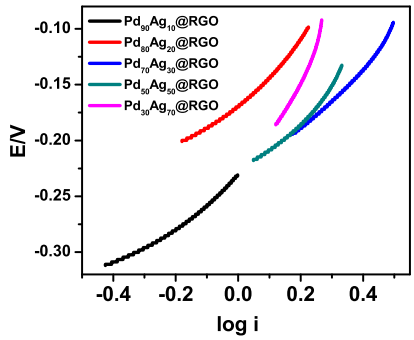

Figure 10. Tafel plots (potential/V vs log of current density) of different Pd_xAg_y@RGO electrodes immersed in 0.1 M butanol in 0.1 M NaOH.

the Tafel region at the lower potential and others at relatively higher potential region, indicating the influence of catalyst composition on the degree of completion of the reaction (on addition of Ag). Both the Tafel slope and i_0 are relatively high for $Pd_{70}Ag_{30}$@RGO in comparison to the others (Table 3).

Table 3. Tafel Slopes and Equilibrium Exchange Current Densities of Different Pd_xAg_y@RGO Nanoalloy Electrodes Immersed in 0.1 M Butan-1-ol in 0.1 M NaOH Solution at Room Temperature

electrodes	slope (b)	intercept (a)	i_0/mA cm^{-2}	i_0/mA mg^{-1}
$Pd_{90}Ag_{10}$@RGO	0.19	0.55	3.72×10^{-7}	15.5×10^{-7}
$Pd_{80}Ag_{20}$@RGO	0.18	0.59	9.77×10^{-8}	44.41×10^{-8}
$Pd_{70}Ag_{30}$@RGO	0.32	1.07	3.61×10^{-6}	24.1×10^{-6}
$Pd_{50}Ag_{50}$@RGO	0.17	0.47	1.92×10^{-7}	14.8×10^{7}
$Pd_{30}Ag_{70}$@RGO	0.07	0.025	1.11×10^{10}	37×10^{10}

Increase of the Tafel slope indicates less value of transmission coefficient for the conversion of butanol to carbonate. This might be due to less availability of catalyst sites for conversion of butanol to butyraldehyde for slow (and less) conversion of the latter upto the end product, carbonate anion. Greater i_0 means greater current density at the equilibrium potential for the abovementioned reaction. Thus, the best current-delivering electrode, $Pd_{70}Ag_{30}$@RGO, increases its current-delivering capability by the formation of more intermediate products rather than progressing toward the end product, carbonate anion. Moreover, both the slope and i_0 are extremely low for the $Pd_{30}Ag_{70}$@RGO electrode because the progress of the reaction upto the end product is slow and time-consuming. For the electrodes having intermediate composition, Tafel slopes and poisoning are also intermediate.

Evidences in Support of the Plausible Mechanism of Butan-1-ol Oxidation for $Pd_{70}Ag_{30}$@RGO Catalyst in 0.1 M NaOH Solution. *CV Study of Sodium Butyrate and Butyraldehyde.* The CV profiles in Figure 11 indicate that the peak currents for the oxidation of Ag metal and Ag_2O and Pd reduction decrease with increase in the concentration of sodium butyrate or butyraldehyde. This suggests that these added compounds get adsorbed on the metal surface, preventing the metal to get oxidized. Moreover, these compounds do not react at the potential range studied. So, this study indicates that sodium butyrate and butyraldehyde do not get oxidized by the electrode at the potential range studied.

DOI: 10.1021/acsomega.8b03561
ACS Omega 2019, 4, 4658−4670

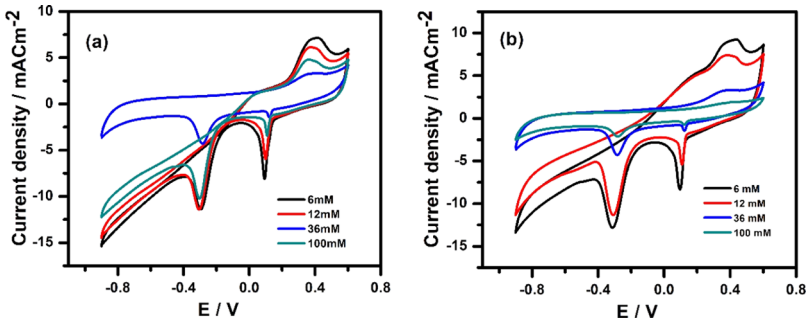

Figure 11. CV profiles of $Pd_{70}Ag_{30}$@RGO catalyst for (a) sodium butyrate and (b) butyraldehyde fuels each at concentrations of 6, 12, 36, and 100 mM in 0.1 M NaOH solution at the scan rate of 50 mV s^{-1}.

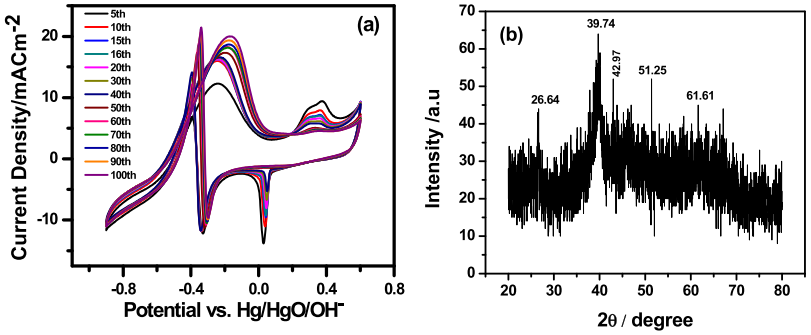

Figure 12. (a) CV profile for butan-1-ol oxidation increases at various cycles for $Pd_{70}Ag_{30}$@RGO catalyst in 0.1 M NaOH solution at the scan rate of 0.05 V/s. (b) XRD profiles of $Pd_{70}Ag_{30}$@RGO catalyst after 100 cycles of voltammetric operation.

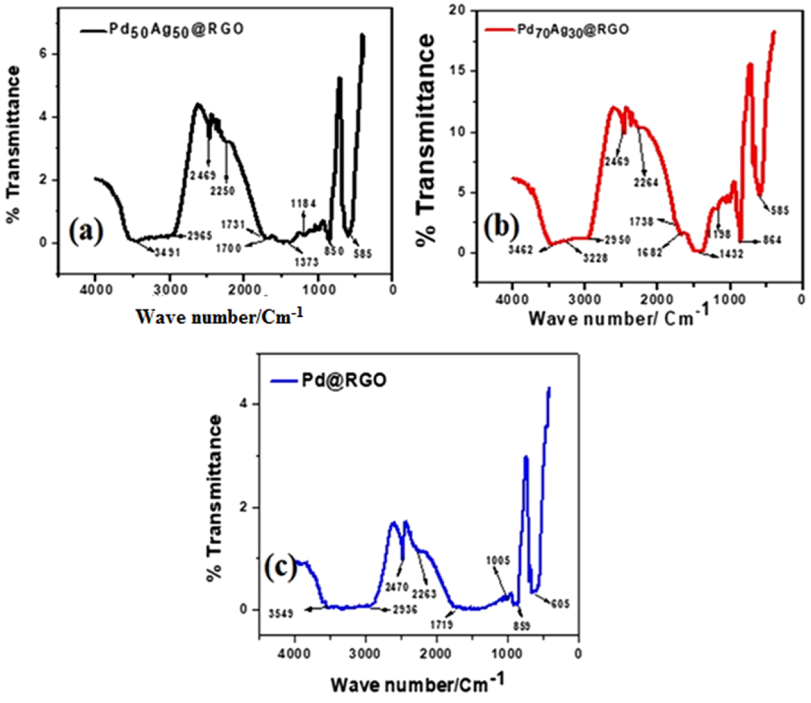

Figure 13. FTIR spectra of (a) $Pd_{50}Ag_{50}$@RGO, (b) $Pd_{70}Ag_{30}$@RGO, and (c) Pd@RGO respectively.

Cycle Study of the Electrocatalysis of Butanol Oxidation on the $Pd_{70}Ag_{30}$@RGO Catalyst. Initially, in the course of oxidation of butanol, Ag adsorbed the fuel to form C_4H_9OAg on the surface of Ag. On repetition of the CV operation, the Ag nanoparticle gets oxidized to form Ag_2O or AgOH, which helps as a secondary catalyst of butan-1-ol oxidation on the Pd−Ag alloy surface. Thus, the peak current density for butanol oxidation increases even after 70 cycles and the peak for Ag to Ag_2O decreases as observed from the CV profile in Figure 12a.

XRD Pattern Study of the Catalyst after 100 Catalytic Cycles. To observe the fate of $Pd_{70}Ag_{30}$@RGO catalyst over the planar carbon surface after the 100th cycle of multiscan CV operation, XRD of the film (Figure 12b) is carried out. It is

DOI: 10.1021/acsomega.8b03561
ACS Omega 2019, 4, 4658−4670

Table 4. Assignments of Main FTIR Bands Observed from the Spectra of the Products of Butan-1-ol Oxidation

$Pd_{70}Ag_{30}$@RGO/C		$Pd_{50}Ag_{50}$@RGO/C		Pd@RGO/C	
wave number cm^{-1}	possible assignment	wave number cm^{-1}	possible assignment	wave number cm^{-1}	possible assignment
2950	C−H symmetrical stretching of $-CH_3$	2965	C−H symmetrical stretching of $-CH_3$	2936	C−H symmetrical stretching of $-CH_3$
1760−1690	butanoate	1697	carbonyl (C═O)	1760−1690	butanoate
1432	deformation of C−H bond	1373	deformation of C−H bond		
864	carbonate	850	carbonate	859	carbonate
1198	symmetrical stretching of C−O bond	1184	symmetrical stretching of C−O bond	1005	$-CH_3$ rocking

seen that the resultant diffractogram contains several spikes because of the presence of amorphous carbon particles; but peaks (2θ/degree) for RGO (26.64°), $Pd_{70}Ag_{30}$@RGO (39.74°), and hexagonal carbon (42.97°), which were present before any CV operation are also vivid here.

The 2θ/degree of $Pd_{70}Ag_{30}$@RGO is slightly decreased, indicating increased interplanar spacing and cell parameter, plausibly due to inclusion of the oxygen atom within the layers of crystallites. Moreover, new peaks for PdO (51.25°) and Ag_2O (61.61°) have generated providing oxidation of the two metals Pd and Ag to a measurable extent, which influence the BOR by being oxygen sources.

FTIR Study. Figure 13 shows the FTIR spectra of $Pd_{50}Ag_{50}$@RGO, $Pd_{70}Ag_{30}$@RGO, and Pd@RGO electrocatalysts after 100 cycles of BOR in alkali. The spectra in each case are very complex showing the presence of numerous peaks that are assigned to adsorption of butanol (reactant) and butaldehyde/butyrate (products) onto the catalyst surface.

However, one noticeable change is observed for the C═O stretching frequencies in each case. Literature reports reveal that generally aldehyde C═O stretching is observed around 1730 cm^{-1}, whereas the carboxylate ions show red-shifted C═O stretching around ∼1700 cm^{-1}. The Pd@RGO catalyst shows (Table 4) carbonyl stretching at 1719 cm^{-1} indicating the merging of the presence of aldehyde and butyrate almost in equal proportions.

However, for $Pd_{50}Ag_{50}$@RGO and $Pd_{70}Ag_{30}$@RGO, two distinct peaks for aldehyde and butyrate, respectively, are observed.

The relative peak intensity of aldehyde is less than the butyrate for the $Pd_{70}Ag_{30}$@RGO catalyst. It is apparent from the above observation that $Pd_{70}Ag_{30}$@RGO accelerates the formation of butyrate. To have detailed information on the relative proportions of the products and reactants, HPLC of the resultant electrolyte solution after 100 cycles has been executed.

HPLC Study of the Product Solution. HPLC study reveals the formation of at least four compounds, as evident from the four intense peaks depicted in Figure 14 for the solutions after BOR on Pd@RGO, $Pd_{50}Ag_{50}$@RGO, and $Pd_{70}Ag_{30}$@RGO electrodes. The compounds produced are sodium butyrate, butyraldehyde, sodium carbonate, and butyl butyrate. HPLC profiles of the first three compounds are also presented here for understanding their peak positions.

It is observed that the retention time (min) of sodium carbonate (6.59) is in between that of butyraldehyde (5.99) and sodium butyrate (7.40). For this reason, although the peak for butyrate in different product solutions is separated and vivid, the peaks for carbonate and butyraldehyde merge together into a single broad peak with or without two humps.

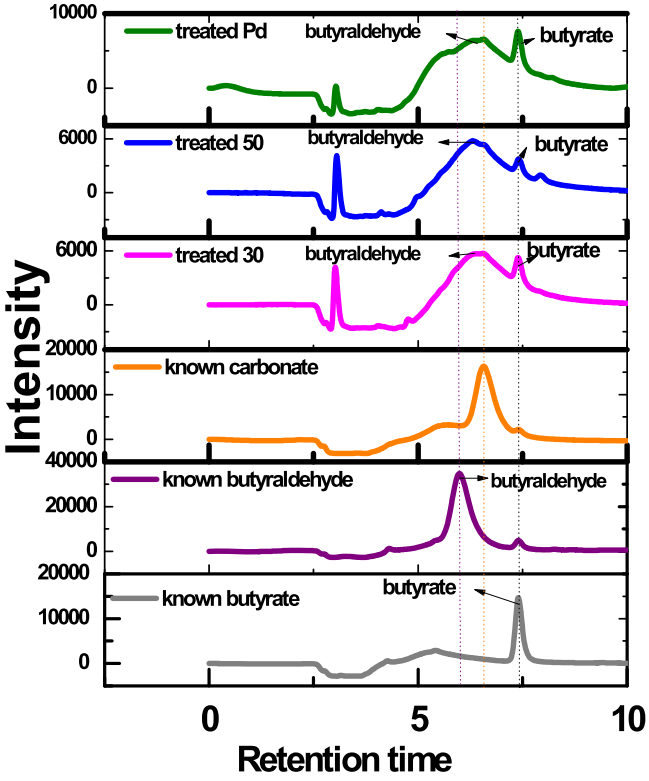

Figure 14. HPLC study of the product solutions of butan-1-ol on Pd@RGO, $Pd_{50}Ag_{50}$@RGO, and $Pd_{70}Ag_{30}$@RGO electrodes.

It is evident from the peak heights (or peak area) that butyl butyrate (3.02) is produced in the order $Pd_{70}Ag_{30}$@RGO (4182) > $Pd_{50}Ag_{50}$@RGO (4032) > Pd@RGO (419), whereas butyraldehyde is produced in the order Pd@RGO (6363) > $Pd_{50}Ag_{50}$@RGO (5839) > $Pd_{70}Ag_{30}$@RGO (5693).

As butyl butyrate is expected to form from a chemical reaction between the produced butyraldehyde and the existing butyl alcohol, its formation can be considered to be equivalent to the formation of butyraldehyde. Thus, it can be told that the initial formation of butyraldehyde is facilitated in the order of catalysts: $Pd_{70}Ag_{30}$@RGO > $Pd_{50}Ag_{50}$@RGO > Pd@RGO. However, the amount of formation of butyrate and carbonate in the studied electrodes follows the order Pd@RGO > $Pd_{70}Ag_{30}$@RGO > $Pd_{50}Ag_{50}$@RGO. It indicates that the subsequent formation of butyrate and carbonate decreases on increasing the mol % of Ag in the composite. Thus, Ag at its optimum composition assists the formation of butyraldehyde but obstructs (prohibits) the formation of butyrate and carbonate at all compositions. This type of conclusion is also obtained in our previous study.[40]

DOI: 10.1021/acsomega.8b03561
ACS Omega 2019, 4, 4658−4670

Scheme 1. Plausible Mechanism of Butan-1-ol Oxidation Reaction

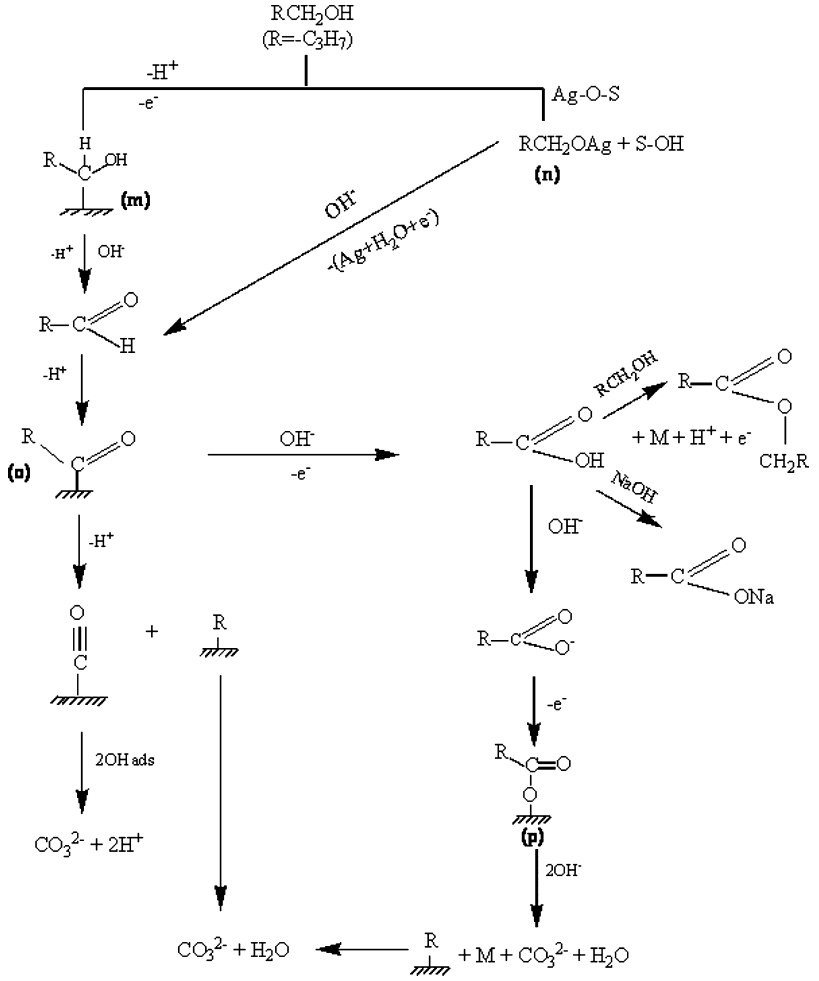

MECHANISM

The CV profile of anodic oxidation of butanol is similar in nature to that of other small alcohols such as methanol and ethanol. Thus, the expected dissociative adsorption of butanol occurs mainly through the C atom rather than the O atom.[40] However, the formation of silver butoxide (RCH_2OAg) at the initial stage cannot be eliminated because it is known that the coinage metal (Au, Ag, or Cu) can form stable alkoxide.[63,64] Silver butoxide can easily lose a H^+, which is abstracted by the alkali, and break the bonding with the Ag atom to form butyraldehyde. As the O−Ag bond dissociation energy is small (221 kJ mol^{-1}), the formation of butyraldehyde, RCHO is expected to be large, greater the content of Ag in Pd_xAg_y alloy. However the produced HCHO may undergo the formation of p or q through "o" or react chemically with butanol to form butyrate. p would form in the presence of more Ag, and q would form in the presence of more Pd. For the $Pd_{70}Ag_{30}$@RGO electrode, formation of both the intermediates p and q will be less, and thus-produced RCHO reacts with RCH_2OH to produce a maximum amount of $RCHOOCH_2R$. FTIR and HPLC studies confirm the presence of butyraldehyde, sodium butyrate, and butyl butyrate in the products. Hence, like methanol[57,65] and ethanol,[66] oxidation of butanol follows a dual path mechanism (Scheme 1) with the formation of adsorbed intermediates (m) and (n). The intermediate (m) subsequently forms butyraldehyde (RCHO) by abstraction of H^+ by OH^-. The intermediate (n) loses a H^+ by reaction with OH_{abs} to produce butyric acid, RCOOH. The butyric acid then reacts with NaOH and butanol RCH_2OH to produce sodium butyrate, $RCOO^-Na^+$, and butyl butanoate ($RCOOCH_2R$). Further adsorption of RCHO on the surface produces intermediates (o) and (p), which on subsequent oxidation produces surface (s)-bound linear CO, S−CO, which on oxidation produces the carbonate anion. The dissociative adsorption of (o) and (p) produces the surface-bound propyl group ($-C_3H_7$), which subsequently oxidizes to carbonate anion and water.

CONCLUSIONS

We have synthesized palladium, silver, and palladium−silver alloy nanoparticles of various binary compositions separately on the RGO matrix by coreduction of the respective metal precursors and GO by hydrazine at 60 °C. The as-synthesized materials, after dropcasting on graphite electrodes, are used as an anode catalyst for butanol oxidation in alkali. Most of the Pd_xAg_y materials exhibit increased and synergic catalytic activity, with $Pd_{70}Ag_{30}$@RGO being the best. Ex situ FTIR and HPLC studies of the products of BOR reveal that butyraldehyde and butyl butyrate are the oxidation products of butanol, whereas the tendency of further oxidation to sodium butyrate or sodium carbonate is reduced by Ag. The best electrode $Pd_{70}Ag_{30}$@RGO is found to be capable of providing a constant peak current even after the 100th cycle of CV operation. Except the expected formation of a little amount of

DOI: 10.1021/acsomega.8b03561
ACS Omega 2019, 4, 4658−4670

PdO and Ag_2O, there is little change in the catalyst material after the 100th cycle of CV operation.

EXPERIMENTAL DETAILS

Reagents. $PdCl_2$ and Nafion (10 mass %) were supplied by Arora Matthey Ltd and Sigma-Aldrich, respectively. Analytical grade reagents such as sodium chloride, potassium chloride, silver nitrate, potassium permanganate, concentrated sulfuric acid, hydrogen peroxide, sodium hydroxide, concentrated hydrochloric acid, sodium butyrate, butyraldehyde, hydrazine, and butan-1-ol were purchased from Merck, India and used without further purification. Deionized water produced by a Milli-Q Ultra-Pure-Water purification system of Millipore was used throughout the experiment. Graphene oxide (GO) was synthesized from ultrafine graphite powder (CDH chemicals) by using a slightly changed Hummer's method.

Synthesis of GO Nanosheets. In a typical method of synthesis, 2.5 g of fine powder of graphite was intimately mixed with 5 g of sodium chloride and taken in a 500 mL beaker placed in an ice bath, followed by slow addition of 50 mL of precooled H_2SO_4. Then, 8 g of $KMnO_4$ was added in steps by taking a small portion each time along with continuous stirring, and the temperature was carefully maintained at 10−15 °C. The stirring was maintained for 2 h followed by slow addition of 250 mL of Millipore water. Such addition of water raised the temperature of the system to ∼90 °C. The mixture was then vigorously agitated at this condition further for about 30 min. To stop unwanted oxidation, an additional 100 mL of Millipore water followed by 30 mL of 30% H_2O_2 solution was added successively that reduced the excess $KMnO_4$. The resultant brown suspension of GO was centrifuged and washed repeatedly with dilute HCl (1:1 (v/v)), Millipore water, and finally, the mass was washed with alcohol and subsequently dried in a vacuum oven at 90 °C.

Synthesis of Graphene-Supported Pd−Ag Bimetallic Nanoparticles. A simultaneous chemical reduction protocol is used for the synthesis of graphene supported Pd−Ag alloy nanoparticles. First, appropriate amounts of solid $PdCl_2$ and KCl (Merck) were first mixed in a 1:2 molar ratio with a little quantity of Millipore water in a 100 mL volumetric flask. The mixture was ultrasonicated for 2 h and kept undisturbed for 24 h. A clean brown solution of K_2PdCl_4 was obtained, and then the volume was made up to the mark to prepare 0.01 M K_2PdCl_4 solution. Then, 0.01 M K_2PdCl_4 and 0.01 M $AgNO_3$ were taken in a round-bottom flask with varying molar (volume) ratios, and a fixed amount of GO was added to each composition and mixed well by constant stirring for 15 min. Then, 1 mL of hydrazine was added to each of the solutions and stirred for 5 min at room temperature. The immediate color change revealed fast generation of nanoparticles with simultaneous reduction of GO to RGO. After setting for 1 h, a black precipitate was obtained. The resultant mass was washed many times with Millipore water, placed in a watch glass, dried by evacuation in about 10 min in an oven kept about at 70 °C, and finally rested in vacuum desiccators. Thus, RGO-supported different nanocomposites of various binary compositions, $Pd_{90}Ag_{10}$@RGO, $Pd_{80}Ag_{20}$@RGO, $Pd_{70}Ag_{30}$@RGO, $Pd_{50}Ag_{50}$@RGO, $Pd_{30}Ag_{70}$@RGO, and Ag@RGO, were obtained following the above procedure. For comparison, separated Pd and Ag nanoparticles supported on RGO, that is Pd@RGO and Ag@RGO, were also synthesized under a similar environment taking the respective precursors.

Characterization. PXRD experiment of the prepared powdered samples was accomplished using a Bruker D8 ADVANCE diffractometer along with a Cu Kα radiation source (λ = 1.5418 Å generated at 40 kV and 40 mA). The surface morphology of the prepared samples was investigated with a SEI INSPECT F 50 FE-SEM microscope. TGA was carried out in a PerkinElmer made system under a N_2 gas atmosphere using 10 °C/min heating rate. Raman spectra was executed in solid state with 514 nm laser excitation via a T64000 Raman system (Make Jobin Yvon HORIBA, France), with an Argon−krypton mixed ion gas laser (2018 RM) (Make Spectra Physics, USA) as the excitation source, optical microscope (BX41) (Make Olympus, Japan) as the collection optic system, and thermoelectric cooled front illuminated 1024 256 CCD, model Synpse TM (Make Jobin Yvon HORIBA, France) as the detector. The electrochemical measurements were carried out using a bicompartment glass cell fitted with the usual three-electrode arrangement at 298.15 K. The reference electrode used in all electrochemical measurements was $Hg/HgO/OH^-$ (1 M) (MMO), whose equilibrium electrode potential was 0.1 V with respect to the normal hydrogen electrode. In all electrochemical measurements, a large Pt foil (1.5 cm × 1.5 cm) was utilized as the auxiliary electrode, and potential data were registered with respect to MMO. CV analysis was executed using a computer-aided potentiostat/galvanostat of AUTOLAB PG STAT 12 (Eco Chemic, Netherlands). Cyclic voltammograms of each electrode immersed in 0.1 M NaOH solution with and without 1-butanol (0.1 M) were recorded at the scan rate 0.05 V s^{-1} for several consecutive cycles until a steady CV curve was found.

ASSOCIATED CONTENT

Supporting Information

The Supporting Information is available free of charge on the ACS Publications website at DOI: 10.1021/acsomega.8b03561.

XRD pattern of all synthesized nanocomposite materials (PDF)

AUTHOR INFORMATION

Corresponding Author

*E-mail: skbhatt7@yahoo.co.in. Phone: +919831699643. Fax: +913324146584.

ORCID

Swapan Kumar Bhattacharya: 0000-0002-1218-1860

Notes

The authors declare no competing financial interest.

ACKNOWLEDGMENTS

The authors acknowledge the Jadavpur University for the infrastructural support and also the DST (INSPIRE Fellowship), New Delhi (IF140929) for the financial support. D.M. acknowledges the Department of Chemistry, Chandernagore College, Hooghly, 712136, WB, India for giving permission for doing honorary research.

REFERENCES

(1) Kirubakaran, A.; Jain, S.; Nema, R. K. A review on fuel cell technologies and power electronic interface. *Renewable Sustainable Energy Rev.* **2009**, *13*, 2430−2440.

DOI: 10.1021/acsomega.8b03561
ACS Omega 2019, 4, 4658−4670

(2) Lamy, C.; Lima, A.; LeRhun, V.; Delime, F.; Coutanceau, C.; Léger, J.-M. Recent Advances in the Development of Direct Alcohol Fuel Cells (DAFC). *J. Power Sources* **2002**, *105*, 283−296.
(3) Sharaf, O. Z.; Orhan, M. F. An overview of fuel cell technology: Fundamentals and applications. *Renewable Sustainable Energy Rev.* **2014**, *32*, 810−853.
(4) Arunkumar, J.; Kalyani, P.; Saravanan, R. Studies on PEM Fuel Cells Using Various Alcohols for Low Power Applications. *Int. J. Electrochem. Sci.* **2008**, *3*, 961−969.
(5) Puthiyapura, V. K.; Brett, D. J. L.; Russell, A. E.; Lin, W.-F.; Hardacre, C. Biobutanol as Fuel for Direct Alcohol Fuel Cells-Investigation of Sn-Modified Pt Catalyst for Butanol Electro-oxidation. *ACS Appl. Mater. Interfaces* **2016**, *8*, 12859−12870.
(6) Kreuer, K. D. On the development of proton conducting polymer membranes for hydrogen and methanol fuel cells. *J. Membr. Sci.* **2001**, *185*, 29−39.
(7) Rousseau, S.; Coutanceau, C.; Lamy, C.; Léger, J.-M. Direct ethanol fuel cell (DEFC): Electrical performances and reaction products distribution under operating conditions with different platinum-based anodes. *J. Power Sources* **2006**, *158*, 18−24.
(8) An, L.; Zhao, T. S.; Shen, S. Y.; Wu, Q. X.; Chen, R. Performance of a direct ethylene glycol fuel cell with an anion-exchange membrane. *Int. J. Hydrogen Energy* **2010**, *35*, 4329−4335.
(9) Takky, D.; Beden, B.; Leger, J. M.; Lamy, C. Evidence for the effect of molecular structure on the electrochemical reactivity of alcohols. *J. Electroanal. Chem. Interfacial Electrochem.* **1983**, *145*, 461−466.
(10) Cao, D.; Bergens, S. H. A direct 2-propanol polymer electrolyte fuel cell. *J. Power Sources* **2003**, *124*, 12−17.
(11) Li, N.-H.; Sun, S.-G.; Chen, S.-P. Studies on the Role of Oxidation States of the Platinum Surface in Electrocatalytic Oxidation of Small Primary Alcohols. *J. Electroanal. Chem.* **1997**, *430*, 57−67.
(12) Chu, Y. H.; Shul, Y. G. Alcohol Crossover Behaviour in Direct Alcohol Fuel Cells (DAFCs) System. *Fuel Cells* **2012**, *12*, 109−115.
(13) Rodrigues, I. d. A.; De Souza, J. P. I.; Pastor, E.; Nart, F. C. Cleavage of the C−C Bond during the Electrooxidation of 1-Propanol and 2-Propanol: Effect of the Pt Morphology and of Co deposited Ru. *Langmuir* **1997**, *13*, 6829−6835.
(14) Colmati, F.; Antolini, E.; Gonzalez, E. R. Preparation, structural characterization and activity for ethanol oxidation of carbon supported ternary Pt−Sn−Rh catalysts. *J. Alloys Compd.* **2008**, *456*, 264−270.
(15) Stevanović, S.; Tripković, D.; Tripković, V.; Minić, D.; Gavrilović, A.; Tripković, A.; Jovanović, V. M. Insight into the Effect of Sn on CO and Formic Acid Oxidation at PtSn Catalysts. *J. Phys. Chem. C* **2014**, *118*, 278−289.
(16) Song, C. Fuel processing for low-temperature and high-temperature fuel cells: Challenges, and opportunities for sustainable development in the 21st century. *Catal. Today* **2002**, *77*, 17−49.
(17) Heinzel, A.; Barragán, V. M. A review of the state-of-the-art of the methanol crossover in direct methanol fuel cells. *J. Power Sources* **1999**, *84*, 70−74.
(18) Habibi, B.; Dadashpour, E. Electrooxidation of 2-propanol and 2-butanol on the Pt−Ni alloy nanoparticles in acidic media. *Electrochim. Acta* **2013**, *88*, 157−164.
(19) Wang, Y.; Zou, S.; Cai, W.-B. Recent Advances on Electro-Oxidation of Ethanol on Pt- and Pd-Based Catalysts: From Reaction Mechanisms to Catalytic Materials. *Catalysts* **2015**, *5*, 1507−1534.
(20) Jiang, L.; Hsu, A.; Chu, D.; Chen, R. Ethanol electro-oxidation on Pt/C and PtSn/C catalysts in alkaline and acid solutions. *Int. J. Hydrogen Energy* **2010**, *35*, 365−372.
(21) Xuan, J.; Leung, M. K. H.; Leung, D. Y. C.; Ni, M. A review of biomass-derived fuel processors for fuel cell systems. *Renewable Sustainable Energy Rev.* **2009**, *13*, 1301−1313.
(22) Antolini, E. Catalysts for direct ethanol fuel cells. *J. Power Sources* **2007**, *170*, 1−12.
(23) Thompson, P. The Agricultural Ethics of Biofuels: The Food vs. Fuel Debate. *Agriculture* **2012**, *2*, 339−358.
(24) Tao, L.; He, X.; Tan, E. C. D.; Zhang, M.; Aden, A. Comparative Techno-Economic Analysis and Reviews of n-Butanol Production from Corn Grain and Corn Stover. *Biofuels, Bioprod. Biorefin.* **2013**, *8*, 342−361.
(25) Dürre, P. Biobutanol: An Attractive Biofuel. *Biotechnol. J.* **2007**, *2*, 1525−1534.
(26) Gandarias, I.; Nowicka, E.; May, B. J.; Alghareed, S.; Armstrong, R. D.; Miedziak, P. J.; Taylor, S. H. The selective oxidation of n-butanol to butyraldehyde by oxygen using stable Pt-based nanoparticulate catalysts: an efficient route for upgrading aqueous biobutanol. *Catal. Sci. Technol.* **2016**, *6*, 4201−4209.
(27) Sakthiselvan, P.; Madhumathi, R.; Partha, N. Eco friendly bio-butanol from sunflower oil sludge with production of xylanase. *Eng. Agric. Environ. Food* **2015**, *8*, 212−221.
(28) Beden, B.; Çetin, I.; Kahyaoglu, A.; Takky, D.; Lamy, C. Electrocatalytic oxidation of saturated oxygenated compounds on gold electrodes. *J. Catal.* **1987**, *104*, 37−46.
(29) Lee, C.-G.; Umeda, M.; Uchida, I. Cyclic voltammetric analysis of C1−C4 alcohol electrooxidations with Pt/C and Pt−Ru/C microporous electrodes. *J. Power Sources* **2006**, *160*, 78−89.
(30) Chen, A.; Ostrom, C. Palladium-Based Nanomaterials: Synthesis and Electrochemical Applications. *Chem. Rev.* **2015**, *115*, 11999−12044.
(31) Zhou, W.; Li, M.; Ding, O. L.; Chan, S. H.; Zhang, L.; Xue, Y. Pd Particle Size Effects on Oxygen Electrochemical Reduction. *Int. J. Hydrogen Energy* **2014**, *39*, 6433−6442.
(32) Wen, C.; Wei, Y.; Tang, D.; Sa, B.; Zhang, T.; Chen, C. Improving the electrocatalytic properties of Pd-based catalyst for direct alcohol fuel cells: effect of solid solution. *Sci. Rep.* **2017**, *7*, 4907.
(33) Dong, Q.; Zhao, Y.; Han, X.; Wang, Y.; Liu, M.; Li, Y. Pd/Cu bimetallic nanoparticles supported on graphene nanosheets: Facile synthesis and application as novel electrocatalyst for ethanol oxidation in alkaline media. *Int. J. Hydrogen Energy* **2014**, *39*, 14669−14679.
(34) Zhang, Y.; Chang, G.; Shu, H.; Oyama, M.; Liu, X.; He, Y. Synthesis of Pt-Pd bimetallic nanoparticles anchored on graphene for highly active methanol electro-oxidation. *J. Power Sources* **2014**, *262*, 279−285.
(35) Kübler, M.; Jurzinsky, T.; Ziegenbalg, D.; Cremers, C. Methanol oxidation reaction on core-shell structured Ruthenium-Palladium nanoparticles: Relationship between structure and electrochemical behaviour. *J. Power Sources* **2018**, *375*, 320−334.
(36) Habibi, B.; Dadashpour, E. Electrooxidation of 2-propanol and 2-butanol on the Pt-Ni alloy nanoparticles in acidic media. *Electrochim. Acta* **2013**, *88*, 157−164.
(37) Gilroy, K. D.; Ruditskiy, A.; Peng, H.-C.; Qin, D.; Xia, Y. Bimetallic nanocrystals: syntheses, properties, and applications. *Chem. Rev.* **2016**, *116*, 10414−10472.
(38) Chen, G.; Xia, D.; Nie, Z.; Wang, Z.; Wang, L.; Zhang, L.; Zhang, J. Facile synthesis of Co-Pt hollow sphere electrocatalyst. *Chem. Mater.* **2007**, *19*, 1840−1844.
(39) Doudna, C. M.; Bertino, M. F.; Blum, F. D.; Tokuhiro, A. T.; Lahiri-Dey, D.; Chattopadhyay, S.; Terry, J. Radiolytic Synthesis of Bimetallic Ag−Pt Nanoparticles with a High Aspect Ratio. *J. Phys. Chem. B* **2003**, *107*, 2966−2970.
(40) Chowdhury, S. R.; Ghosh, S.; Bhattachrya, S. K. Improved Catalysis of Green-Synthesized Pd-Ag Alloy-Nanoparticles for Anodic Oxidation of Methanol in Alkali. *Electrochim. Acta* **2017**, *225*, 310−321.
(41) Majumdar, D.; Baugh, N.; Bhattacharya, S. K. Ultrasound assisted formation of reduced graphene oxide-copper (II) oxide nanocomposite for energy storage applications. *Colloids Surf., A* **2017**, *512*, 158−170.
(42) Majumdar, D.; Bhattacharya, S. K. Sonochemically synthesized hydroxy-functionalized graphene−MnO2nanocomposite for super-capacitor applications. *J. Appl. Electrochem.* **2017**, *47*, 789−801.
(43) Wu, P.; Huang, Y.; Zhou, L.; Wang, Y.; Bu, Y.; Yao, J. Nitrogen-doped graphene supported highly dispersed palladium-lead nano-

DOI: 10.1021/acsomega.8b03561
ACS Omega 2019, 4, 4658−4670

particles for synergetic enhancement of ethanol electrooxidation in alkaline medium. *Electrochim. Acta* **2015**, *152*, 68−74.
(44) Yang, L.; Ding, Y.; Chen, L.; Luo, S.; Tang, Y.; Liu, C. Hierarchical reduced graphene oxide supported dealloyed platinum−copper nanoparticles for highly efficient methanol electrooxidation. *Int. J. Hydrogen Energy* **2017**, *42*, 6705−6712.
(45) Li, L.; Chen, M.; Huang, G.; Yang, N.; Zhang, L.; Wang, H.; Liu, Y.; Wang, W.; Gao, J. A green method to prepare Pd−Ag nanoparticles supported on reduced graphene oxide and their electrochemical catalysis of methanol and ethanol oxidation. *J. Power Sources* **2014**, *263*, 13−21.
(46) Gong, M.; Yao, Z.; Lai, F.; Chen, Y.; Tang, Y. Platinum−copper alloy nanocrystals supported on reduced graphene oxide: One-pot synthesis and electrocatalytic applications. *Carbon* **2015**, *91*, 338−345.
(47) Liu, J.; Zhou, H.; Wang, Q.; Zeng, F.; Kuang, Y. Reduced graphene oxide supported palladium−silver bimetallic nanoparticles for ethanol electro-oxidation in alkaline media. *J. Mater. Sci.* **2011**, *47*, 2188−2194.
(48) Wang, Y.; Sheng, Z. M.; Yang, H.; Jiang, S. P.; Li, C. M. Electrocatalysis of carbon black- or activated carbon nanotubes-supported Pd-Ag towards methanol oxidation in alkaline media. *Int. J. Hydrogen Energy* **2010**, *35*, 10087−10093.
(49) Li, G.; Jiang, L.; Jiang, Q.; Wang, S.; Sun, G. Preparation and characterization of Pd_xAg_y/C electrocatalysts for ethanol electro-oxidation reaction in alkaline media. *Electrochim. Acta* **2011**, *56*, 7703−7711.
(50) Kakaei, K.; Dorraji, M. One-pot synthesis of Palladium Silver nanoparticles decorated reduced graphene oxide and their application for ethanol oxidation in alkaline media. *Electrochim. Acta* **2014**, *143*, 207−215.
(51) Yang, J.; Zhou, Y.; Su, H.; Jiang, S. Theoretical study on the effective methanol decomposition on Pd (111) surface facilitated in alkaline medium. *J. Electroanal. Chem.* **2011**, *662*, 251−256.
(52) Mandal, K.; Bhattacharjee, D.; Roy, P. S.; Bhattacharya, S. K.; Dasgupta, S. Room temperature synthesis of Pd−Cu nanoalloy catalyst with enhanced electrocatalytic activity for the methanol oxidation reaction. *Appl. Catal., A* **2015**, *492*, 100−106.
(53) Banik, S.; Mahajan, A.; Chowdhury, S. R.; Bhattacharya, S. K. Improved and synergistic catalysis of single-pot-synthesized Pt−Ni alloy nanoparticles for anodic oxidation of methanol in alkali. *RSC Adv.* **2016**, *6*, 92490−92501.
(54) Xu, L.; Luo, Z.; Fan, Z.; Yu, S.; Chen, J.; Liao, Y.; Xue, C. Controllable Galvanic Synthesis of Triangular Ag−Pd Alloy Nanoframes for Efficient Electrocatalytic Methanol Oxidation. *Chem.—Eur. J.* **2015**, *21*, 8691−8695.
(55) Chowdhury, S. R.; Bera, K. K.; Bhattacharya, S. K. Enhanced and Synergistic Catalysis of Green Synthesized Pd-Ag Alloy Nanoparticles for Anodic Oxidation of Propan-2-ol in Alkali. *Mater. Today: Proc.* **2018**, *5*, 2171−2178.
(56) Hammer, B.; Nørskov, J. K. Theoretical surface science and catalysis—calculations and concepts. *Adv. Catal.* **2000**, *45*, 71−129.
(57) Chowdhury, S. R.; Mukherjee, P.; Bhattachrya, S. k. Palladium and palladium−copper alloy nano particles as superior catalyst for electrochemical oxidation of methanol for fuel cell applications. *Int. J. Hydrogen Energy* **2016**, *41*, 17072−17083.
(58) Jasuja, K.; Berry, V. Implantation and growth of dendritic gold nanostructures on graphene derivatives: electrical property tailoring and raman enhancement. *ACS Nano* **2009**, *3*, 2358−2366.
(59) Lin, Y.; Watson, K. A.; Fallbach, M. J.; Ghose, S.; Smith, J. G., Jr.; Delozier, D. M.; Cao, W.; Crooks, R. E.; Connell, J. W. Rapid, solvent less, bulk preparation of metal nanoparticle-decorated carbon nanotubes. *ACS Nano* **2009**, *3*, 871−884.
(60) Yang, S.; Dong, J.; Yao, Z.; Shen, C.; Shi, X.; Tian, Y.; Lin, S.; Zhang, X. One-Pot Synthesis of Graphene-Supported Monodisperse Pd Nanoparticles as Catalyst for Formic Acid Electro-oxidation. *Sci. Rep.* **2014**, *4*, 4501−4506.
(61) Chowdhury, S. R.; Roy, P. S.; Bhattacharya, S. K. Green synthesis and characterization of polyvinyl alcohol stabilized palladium nanoparticles: Effect of solvent on diameter and catalytic activity. *Adv. Nat. Sci.: Nanosci. Nanotechnol.* **2017**, *8*, 025002.
(62) Bagchi, J.; Bhattacharya, S. K. Studies of the electro-catalytic activity of binary palladium ruthenium anode catalyst on Ni support for ethanol alkaline fuel cells. *Transition Met. Chem.* **2007**, *33*, 113−120.
(63) Batista, E. A.; Malpass, G. R. P.; Motheo, A. J.; Iwasita, T. New mechanistic aspects of methanol oxidation. *J. Electroanal. Chem.* **2004**, *571*, 273−282.
(64) Rodriguez, P.; Kwon, Y.; Koper, M. T. M. The promoting effect of adsorbed carbonmonoxide on the oxidation of alcohols on a gold catalyst. *Nat. Chem.* **2011**, *4*, 177−182.
(65) Mahajan, A.; Banik, S.; Roy, P. S.; Chowdhury, S. R.; Bhattacharya, S. K. Kinetic parameters of anodic oxidation of methanol in alkali: Effect of diameter of Pd nano-catalyst, composition of electrode and solution and mechanism of the reaction. *Int. J. Hydrogen Energy* **2017**, *42*, 21263−21278.
(66) Mukherjee, P.; Roy, P. S.; Mandal, K.; Bhattacharjee, D.; Dasgupta, S.; Bhattacharya, S. K. Improved catalysis of room temperature synthesized Pd-Cu alloy nanoparticles for anodic oxidation of ethanol in alkaline media. *Electrochim. Acta* **2015**, *154*, 447−455.

DOI: 10.1021/acsomega.8b03561
ACS Omega 2019, 4, 4658−4670